Bodies-of-revolution in turbulent flow: comparing computation with experiment

Michel Visonneau, Ganbo Deng, Emmanuel Guilmineau, Liuyang Ding, Alexander J Smits

Bodies-of-revolution in turbulent flow: comparing computation with experiment

Michel Visonneau*, Ganbo Deng†, Emmanuel Guilmineau‡
CNRS - LHEEA (Centrale Nantes), France

Liuyang Ding§, Alexander J. Smits¶
Princeton University, Princeton, New Jersey 08544, U.S.A.

This paper is part of the Special Session organized to report progress made by NATO AVT-349 RTG on the topic of Non-Equilibrium Turbulent Boundary Layers at High Reynolds Number. The aim of this effort is to develop opportunities for collaboration between NATO researchers in the area of non-equilibrium turbulent boundary layers in high Reynolds number flows at incompressible conditions including, specifically, effects of surface roughness, curvature, favourable and adverse pressure gradients, and three-dimensionality. A particular aim is to foster joint experimental and computational studies of such flows with a view to developing improved turbulence models, low order prediction methods for design and control, and physical understanding. Here, we report progress on the experiments and computations of the test case where a body-of-revolution is placed on the centerline of fully-developed turbulent pipe flow, thereby imposing on the turbulence the effects of pressure gradients, streamline curvature, and flow divergence and convergence. In addition, the test case encompasses the far-wake where the turbulence relaxes to its equilibrium conditions, albeit very slowly.

Nomenclature

Re_D	=	bulk flow Reynolds number, $Re = U_b D/\nu$
Re_τ	=	friction Reynolds number, $Re = u_\tau R/\nu$
D	=	pipe diameter
R	=	pipe radius
d	=	body diameter (in the mid-body portion)
U_b	=	bulk velocity
u_τ	=	friction velocity, $u_\tau = \sqrt{\tau_w/\rho}$
τ_w	=	wall shear stress
ν	=	kinematic viscosity
ρ	=	fluid density
x	=	streamwise distance measured from bow
$\overline{\ }$	=	(accent) time or ensemble average

I. Introduction

Here, we report progress on the experiments and computations of the AVT-349 test case where a body-of-revolution is placed on the centerline of a fully-developed turbulent pipe flow, thereby imposing on the turbulence the effects of

*CNRS Research Director - LHEEA (Centrale Nantes), France
†Centrale Nantes Senior Research Associate - LHEEA (Centrale Nantes), France
‡CNRS Senior Research Associate - LHEEA (Centrale Nantes), France
§Postdoctoral Fellow, Mechanical and Aerospace Engineering, Princeton University, Princeton NJ.
¶Eugene Higgins Professor, Mechanical and Aerospace Engineering, Princeton University, Princeton NJ, AIAA Fellow.

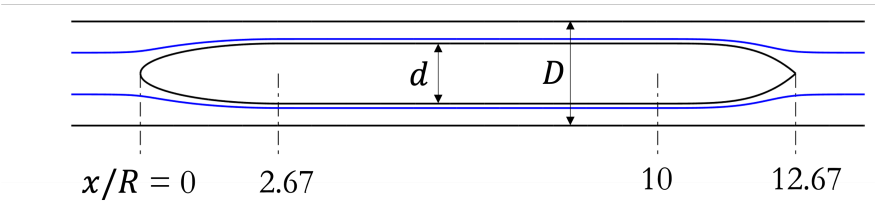

Fig. 1 Test section geometry. Three body diameters were tested, i.e. d/D = 1/3, $\sqrt{2}/3$ and $\sqrt{3}/3$. Blue solid lines are selected streamlines from a potential flow calculation. Flow is from left to right.

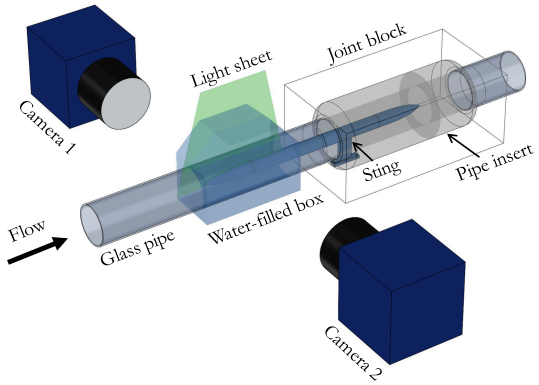

Fig. 2 Schematic of the experimental set-up for measurement in the bow section plus part of the mid-body region (x/R < 5.5). For the stern region and the wake, only one camera was employed with a similar magnification at locations up to 40R downstream of the stern.

pressure gradients, streamline curvature, and flow divergence. In addition, the test case encompasses the far-wake where the turbulence relaxes to its equilibrium conditions, albeit very slowly.

The experiments and some preliminary computations were performed at Princeton University [1], while the primary computations were conducted at the CNRS Research Laboratory in Hydrodynamics, Energetics and Atmospheric Environment (LHEEA) in Nantes, France. There are three test cases, for different blockage ratios, at a fixed Reynolds number $Re_D = U_b D/\nu = 156,000$ ($Re_\tau = 3550$). Only the results for the medium blockage case where the area ratio was 2/9 ($d/D = \sqrt{2}/3$) are reported here. The computations were performed using a finite volume RANS approach on unstructured meshes [2].

II. Experiment

A. Experimental methods

Figure 1 illustrates the test configuration. A streamlined axisymmetric body was placed on the centerline of a long pipe that has an inner diameter of $D = 2R = 38.1$ mm. The body consisted of three parts – the bow section ($0 < x/R < 2.67$), the cylindrical recovery section ($2.67 < x/R < 10$), and the stern section ($10 < x/R < 12.67$). The bow section is a half prolate spheroid , the recovery section has a constant diameter d, and the contour of the stern follows a 4th-order power law to minimize the drag [3]. The body was rigidly supported by an aerodynamically shaped sting (NACA 0015) (more detail of the set-up is given in Ding et al. [1]). Three body diameters, d/D = 1/3, $\sqrt{2}/3$ and $\sqrt{3}/3$, were chosen to vary the magnitude and rate of change of pressure, divergence and curvature, and the results for the medium body are compared to computations in the current work. The inflow was ensured to be fully-developed turbulent pipe flow by allowing 200D of development length upstream of the body. The presence of the body causes the incoming turbulent pipe flow to experience a favorable pressure gradient (FPG), streamline divergence and convex curvature over the bow, followed by a relaxation over the recovery section, and an adverse pressure gradient (APG), streamline

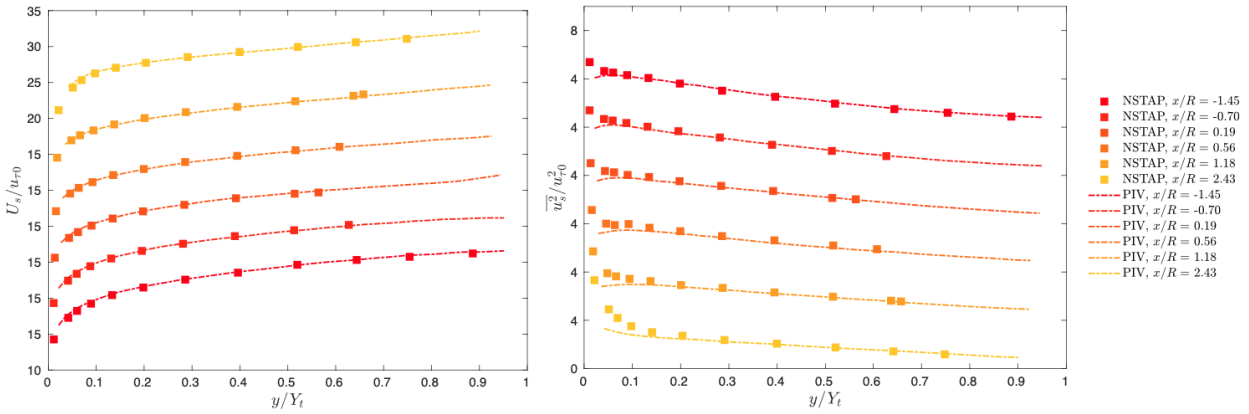

Fig. 3 Comparison of PIV results with NSTAP data for mean velocity and turbulence intensity in the bow section. For PIV, Re_D = 163000; for NSTAP, Re_D = 202000. Here, y is measured from the pipe wall, and Y_t is the distance between the pipe and body walls. The origin of each profile is shifted up by 5 (mean velocity, left) or 4 (turbulence intensity, right) to elucidate the comparisons.

convergence, and convex curvature over the stern region. Far downstream the flow then slowly recovers to its initial state.

The upstream fully developed flow had a bulk velocity $U_b \approx 4.1$ m/s, corresponding to $Re_D = U_b D/\nu \approx 156{,}000$, where $\nu = 10^{-6}$ is the kinematic viscosity of water at 20°C. Using the friction factor correlation reported by [4], the upstream friction velocity was determined to be $u_\tau = 0.186$ m/s, and $Re_\tau = u_\tau R/\nu = 3550$.

The mean flow and Reynolds stress development and recovery were characterized in two measurement campaigns using particle image velocimetry (PIV) in the axial-radial plane on the opposite side of the sting. The flow in the anterior section of the body (bow and mid-body up to $x/R = 5.5$) was measured in the first campaign with a set-up shown schematically in figure 2. Two cameras (LaVision Imager sCMOS) offset in the axial direction were positioned on opposite sides of the pipe to simultaneously achieve high spatial resolution and an extended field of view. A 2× teleconverter (Vivitar) was attached to each camera to further enhance the resolution, leading to a magnification of 0.54 (83 pix/mm). A water-filled box was sealed around the pipe to alleviate image distortion due to unmatched indices of refraction. Images were taken at two locations so that the full field of view encompassed the region up to x/R = 5.5. First- and second-order flow statistics were calculated from 20,000 image pairs at each station and an in-house particle tracking code based on the non-iterative algorithm developed by Fuchs et al. [5]. Flow statistics at desired grid points were then calculated by averaging velocities of individual particles within a small volume [6, 7]. The final spatial resolution is 0.8 mm (streamwise) × 0.4 mm (stream normal).

The second PIV campaign was conducted to measure the flow in the stern region and the wake at multiple stations ($8.5 < x/R < 52$). The experimental procedure was similar to that described in Ding and Smits [8], except that a 20 mm extension ring was used to achieve a magnification of 0.49 (75 pix/mm), matching that in the bow section. 10,000 image pairs were recorded at each station and processed using the multi-grid iterative image deformation algorithm in DaVis 8.3 with a final spatial resolution of 0.43 mm × 0.43 mm and 50% window overlap.

B. Validity of PIV data

Before making comparisons between computation and experiment, the accuracy of the experimental data needs to be assessed. Figure 3 compares PIV results in the bow section with those obtained using a NSTAP sensor [10] in the Princeton Superpipe at a similar Reynolds number. The NSTAP sensor is a nano-scale hot-wire probe with a sensing length of $l^+ \approx 3$ (l = 60 μm) for this Reynolds number, yielding minimal spatial filtering effects for resolving small-scale motions. As seen in the left panel of figure 3, the agreement of the mean velocity is exceptional with a maximum deviation of approximately 1%. For the streamwise turbulence intensity, shown in the right panel of figure 3, while the agreement is satisfactory for $y/Y_t > 0.15$ (Y_t is the distance between the pipe and body walls), the spatial filtering inherent in PIV leads to an underestimation of $\overline{u^2}$ in the near-wall region. As an extreme example, at x/R = 2.43 and $y/Y_t = 0.05$, PIV only resolves about 60% of the energy measured by NSTAP.

The spatial filtering of PIV is further made clear by comparison with DNS results of the upstream turbulent pipe flow at a slightly lower Reynolds number, as presented in figure 4. Again, we see good agreement for the mean velocity

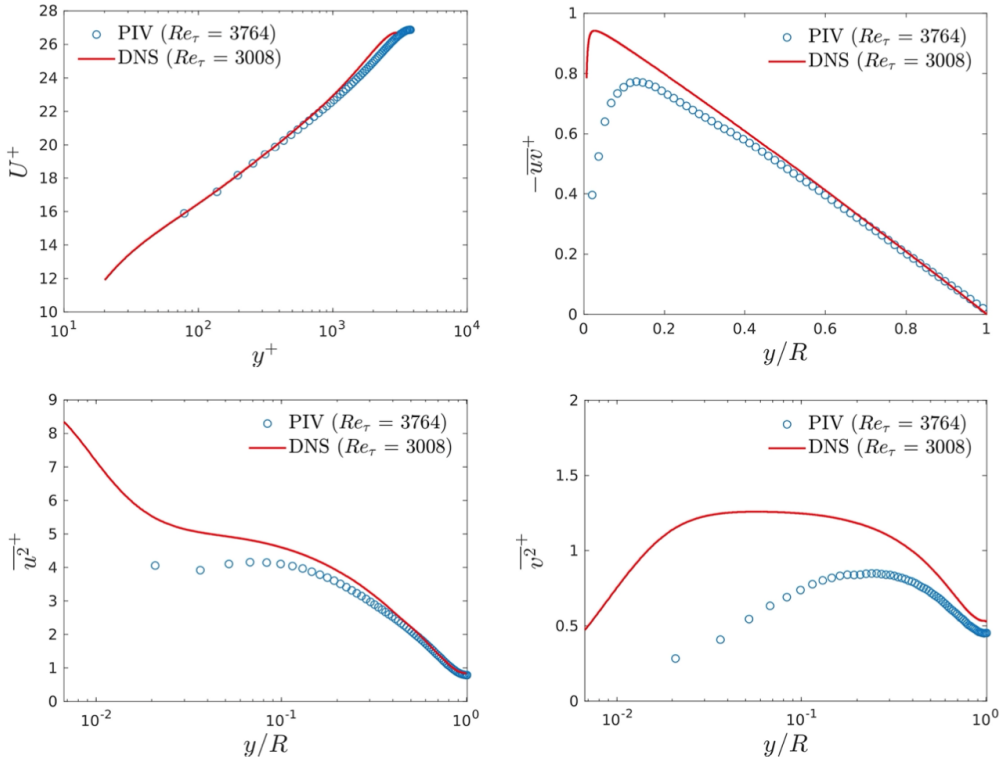

Fig. 4 Comparison of PIV results with DNS data for mean velocity and turbulence intensity in the bow section. For PIV, Re_D = 166000; for DNS, Re_D = 133000. DNS data taken from [9].

(except for some small differences in the wake due to unmatched Reynolds numbers), whereas all three Reynolds stresses are subjected to noticeable spatial filtering effects near the wall. Farther from the wall, the effects quickly moderate, and for $y/R > 0.2$ $-\overline{uv}$ and $\overline{u^2}$ the maximum deviation is $< 8\%$. For $\overline{v^2}$, strong attenuation is observed over most of the pipe cross section where small-scale wall-normal fluctuations are significant.

The above comparisons suggest that the mean velocity measured by PIV is a reliable source to compare to, whereas comparisons of turbulent stresses will need to take into account the effects of spatial filtering in the near-wall regions.

III. Computation

A. Flow solvers used in this study

The computations were performed with two different solvers. The first one is the in-house solver ISIS-CFD developed by the French authors, also available as a part of the FINE™/Marine computing suite worldwide distributed by Cadence Design Systems. ISIS-CFD is an incompressible multiphase unsteady Reynolds-averaged Navier-Stokes (URANS) solver mainly devoted to marine hydrodynamics. It is based on a fully-unstructured (face-based) finite volume discretization with specific functionalities needed for multiphase flows and industrial applications [2, 11]. The method features several sophisticated turbulence models: apart from the classical two-equation k-ϵ and k-ω models, the anisotropic two-equation Explicit Algebraic Reynolds Stress Model (EARSM), as well as Reynolds Stress Transport Models, are available [12–14]. All models are available with wall-function or low-Reynolds near wall formulations. Hybrid RANS/LES turbulence models based on Detached Eddy Simulation (DES-SST, DDES-SST, IDDES) are also implemented and have been thoroughly validated on automotive flows characterized by large separations [15] and ships at steady drift [16]. Moreover, the solver accepts sliding and overset grids and features an anisotropic adaptive grid refinement functionality ([17], [18]) applied to unstructured hexahedral meshes.

Two different turbulence models have been selected for the simulations shown in this present study. The first one is the well known linear isotropic k-ω SST model by Menter [19]. The second one is a Reynolds stress transport model

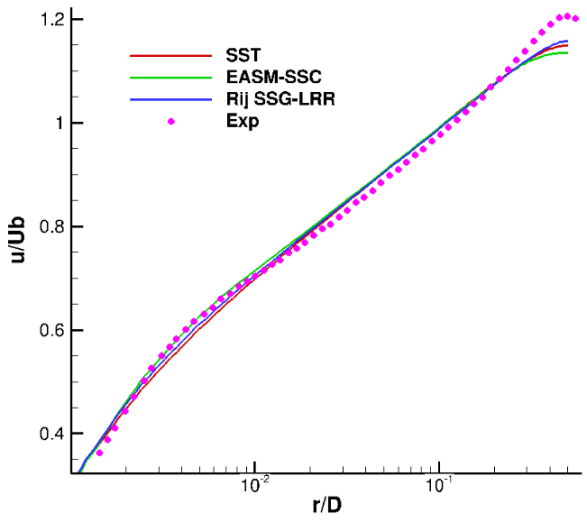

Fig. 5 Axial velocity profiles u/U_b for the inlet condition. Experiment is at $Re_D = DU_b/\nu$ = 144580; computation is at Re_D = 156000.

based on the SSG-LRR pressure-strain model [14].

The second solver used by the American authors is OpenFOAM (v6). The Reynolds-averaged momentum equation combined with Menter's $k-\omega$ SST model was solved using the SIMPLE algorithm provided in OpenFOAM for a steady flow solution. The computation domain started from $4d$ upstream of the bow and extended to $8d$ downstream of the stern. The inflow condition was generated from DNS data of a fully developed pipe flow at $Re_\tau = 3008$ [9]. A 5° wedge with periodic boundary conditions was used to simulate the axisymmetric flow, and a structured mesh containing 387K hexaheldral cells was generated with the OpenFOAM built-in mesh generator, blockMesh. The computation was wall-resolved with the first grid point located at $y^+ \approx 0.5$, and a normalized residual of 10^{-6} was specified to ensure sufficient accuracy and convergence.

B. Computational setup

First, a computation of fully developed pipe flow at the same Reynolds number was performed to obtain the inlet condition for the simulation. When the computed mean velocity profile is compared with the fully developed profile obtained in the Princeton Superpipe facility at a similar Reynolds number [20], a noticeable difference is observed in the wake region. See figure 5. The experimental velocity profile rises above the law of the wall at about $y = 0.2D$, signalling the start of the wake region, with a wake strength that is consistent with past experience [21]. In contrast, the CFD prediction continues to follow the law of the wall until about $y = 0.3D$, then deviates from it to form a wake with a considerably lower wake strength. At the center of the pipe, the axial velocity u normalized by the bulk velocity U_b is about 1.206 in the measurements, while in the computations it is about 1.1495 with the SST model and 1.1570 with the SSG-LRR model. This under-estimation of the axial velocity near the center of the pipe (about 5%) is a discrepancy that needs to be taken into account when comparing the CFD and experimental results over the body.

A 2D mesh containing 139K cells is generated with the unstructured hexahedral mesh generator Hexpress. It is transformed to fit to the axisymmetric configuration covering a section of 0.8°. The distance to the wall of the first cell is about 4 10^{-6}, giving a y^+value lower than 0.02, small enough for a computation using a no-slip wall boundary condition. The computation is performed using Cartesian velocity components with appropriate boundary conditions. A coarser grid around the body containing 85K cells gives almost the same results indicating that the numerical uncertainty is low enough. A 3D computation covering the whole domain containing more than 10M cells has also been performed for further verification. It indicates that three-dimensional effects are negligible and also provides the same results as the computations mentioned above.

The CFD results are compared to measurement data for the axial velocity and the shear stress in figures 6 to 9, for four different regions from the bow to the wake: the bow, the center body, the stern, and the wake.

For the bow region (figure 6), the first profile is located at $x = -0.1R$. At this location, the measurement data for

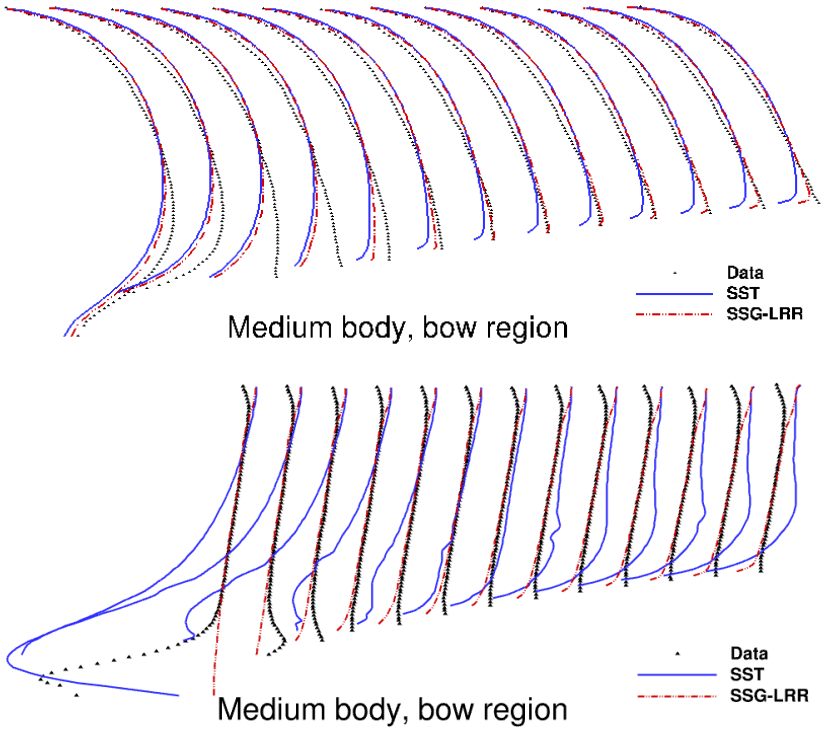

Fig. 6 Bow region. Top: axial velocity profiles. Bottom: shear stress profiles. Profiles are shown from x/R = -0.1 to x/R = 1.1 with a 0.1R increment.

axial velocity near the center of the pipe is higher than the CFD prediction, most likely because of the differences in the inlet profiles seen in figure 5. The SST model over-predicts the turbulence kinetic energy near the stagnation point, resulting in too high a shear stress and a very thick turbulent boundary layer. This is a well known fault of linear isotropic eddy-viscosity models. At this station, the shear stress obtained by the measurement is relatively high, while with the Reynolds stress SSG-LRR turbulence model, the shear stress is very small. It is important to have additional, highly-resolved measurements in the region just upstream of the bow. Such measurements are currently underway using NSTAP probes in the Princeton Superpipe [22].

The shear stress measurements at the next two stations in the bow region reveal a surprising result. Here, the shear stress has an opposite sign compared with its behavior in a typical boundary layer, which means that there is an energy transfer from turbulence kinetic energy to mean momentum energy of the flow. Instead of decelerating the flow in this region, the turbulent shear stress accelerates the flow. This can be clearly observed from the rapid increase of axial velocity near the body from station 2 ($x/R = 0$) to station 3 ($x/R = 0.1$) which is completely missed by the CFD simulation with either turbulence model. Further downstream, there is a distinct difference between the two predictions, where the Reynolds stress model shows a much faster acceleration near the wall. Starting from station 7 (located at $x = 0.5R$), a good agreement for the axial velocity between the CFD and the measurement is observed near the body, but the shear stress levels display noticeable differences. The better prediction obtained with the Reynolds stress transport equation model can be explained by the fact that it takes into account the transport effect of the Reynolds stress which has an important impact in momentum transport near a curved surface.

For the center body region (figure 7), the differences between the CFD prediction and the measurement data are mainly due to the discrepancies observed in the upstream region propagating downstream. The thickness of the boundary layer grows too quickly even when the Reynolds stress transport equation model is employed. In the main flow region between the two walls, the shear stress predicted by the SSG-LRR model agrees much better with the measurement data compared with the prediction given by the k-ω SST model. Near the wall, the shear stress in the measurement is much smaller than the CFD prediction. This may be exacerbated by the spatial resolution issues in the PIV data, as discussed earlier.

In the stern region (figure 8), the consequences of the poor predictions by CFD in the bow region become smaller.

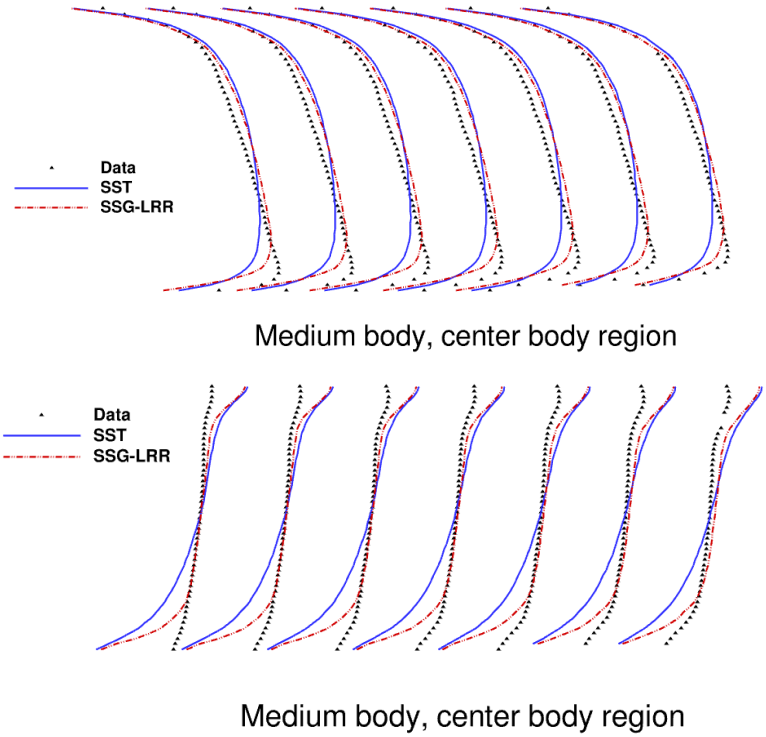

Fig. 7 Center body. Top: axial velocity profiles. Bottom: shear stress profiles. Profiles are shown from x/R = 4.17 to x/R = 5.37 with a 0.2R increment.

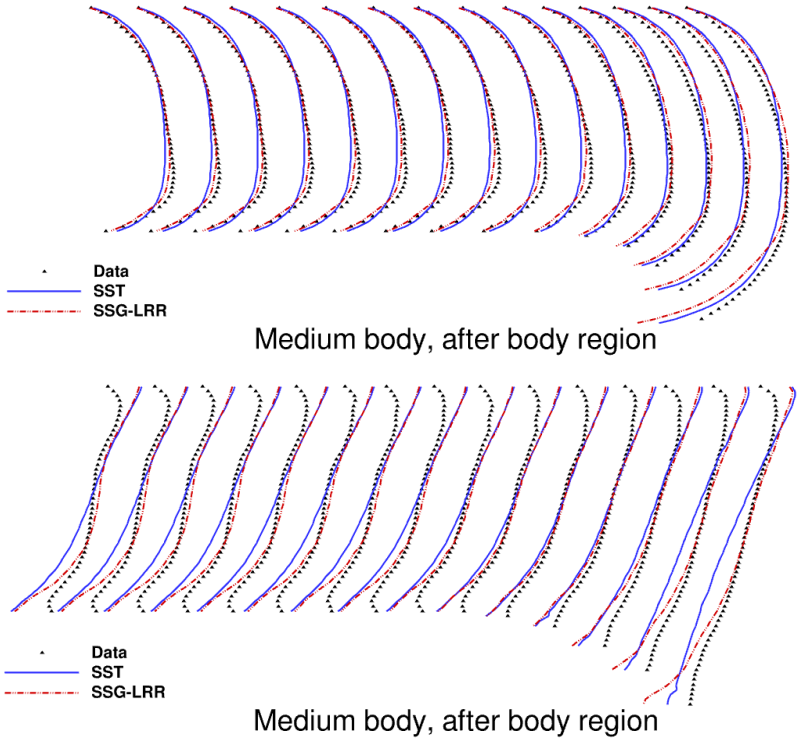

Fig. 8 Stern region. Top: axial velocity profiles. Bottom: shear stress profiles. From station x/R=8.67 to station x/R=12.17 with a 0.25R increment.

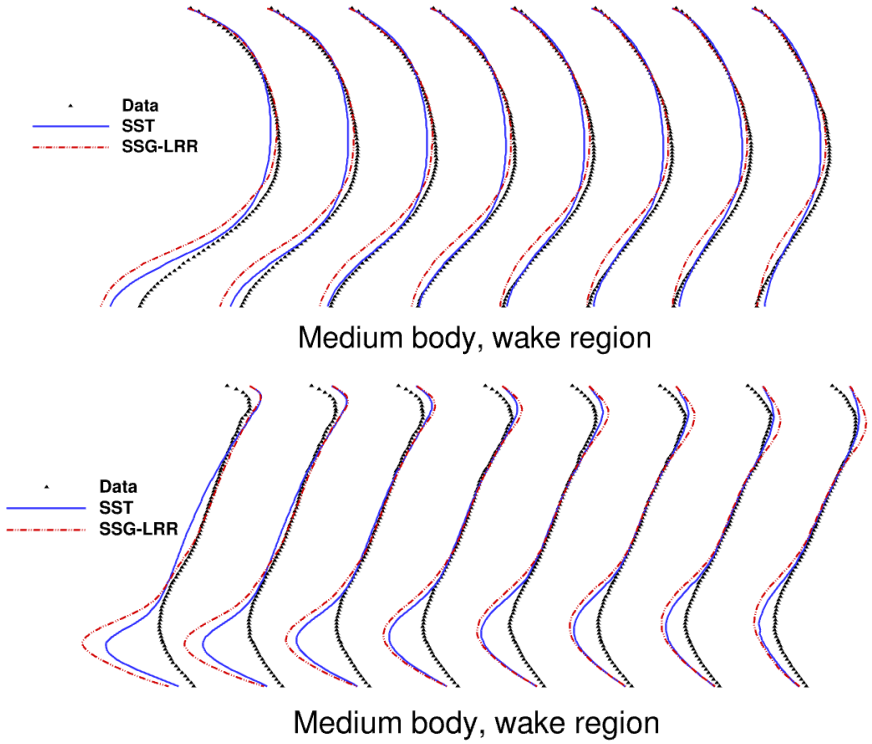

Fig. 9 Wake region. Top: axial velocity profiles. Bottom: shear stress profiles. From station x/R=12.9167 to station x/R=16.4167 with a 0.5R increment.

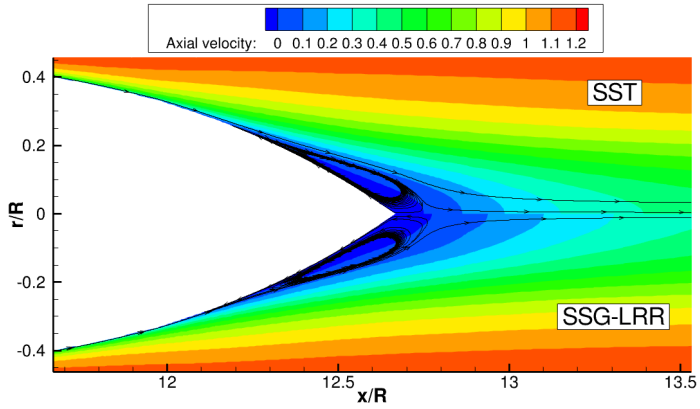

Fig. 10 Wake region. Predicted streamlines with contours of axial velocity magnitude.

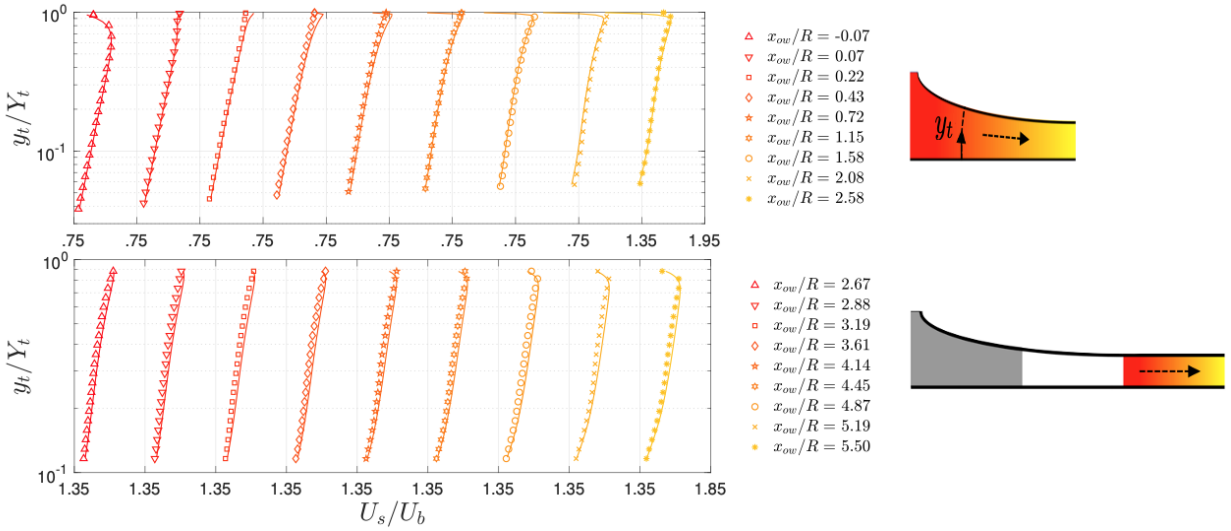

Fig. 11 Preliminary computations using OpenFOAM v6 with the k-ω-SST model by [19]. Mean flow comparisons over the bow and mid-body of the case with $d/D = 1/3$.

Both turbulence models can provide a prediction in relatively good agreement for the axial velocity in this region. At the first stations in this region, the SSG-LRR model provides a better prediction both for the axial velocity and for the shear stress, especially near the surface of body. But at the farthest downstream sections, additional discrepancies are observed in the predicted axial velocity given by the SSG-LRR model, where near the wall the predicted shear stress is always much larger than the experimental values. The spatial resolution of the PIV is about the same as in the bow region, so undoubtedly the measurements underestimate the actual shear stress levels to some extent in this region.

In the wake region (figure 9), it is the SST model that provides the best prediction for the axial velocity. The under-estimation of axial velocity near the wall of the pipe observed in upstream locations is no longer observed. However, the predicted shear stress remains much higher than the experimental values, even near the center of the pipe where possible interference due to the wall in the measurement can be excluded. It should be noted that the strong shear layer in the immediate wake of the body is not fully resolved by PIV.

Both turbulence models predict a flow re-circulation zone in the wake as shown in figure 10, while it is not observed in the measurement. In addition to possible turbulence modelling errors in the after body region, the under-estimation of axial velocity near the body in the upstream region may also have an impact. Momentum energy in the boundary layer near the wall is higher everywhere in the measurement compared to the CFD.

Some preliminary results obtained using OpenFOAM (v6) with the $k-\omega$ SST model are given in figure 11 for the mean flow over the bow and mid-body of the case with $d/D = 1/3$. The shear stress results in the same region are shown in figure 12. Here, flow statistics are compared based on a streamline coordinate system consisting of mean streamlines and stream-normal lines. Despite the difference in coordinate systems, the comparisons between measurement and computation are very similar to those discussed earlier. The agreement of the mean streamwise velocity is overall good except near the initial part of the bow. The shear stress comparison shows considerable deviations, where the SST model overpredicts the development of turbulence near the body wall, resulting in a much thicker boundary layer.

IV. Conclusions

Comparisons between CFD simulations and the PIV measurements reveal that the initial response of the upstream turbulent flow to the presence of body and its subsequent acceleration around the body is the most challenging turbulence modelling task for the RANSE approach in this configuration. Due the strong pressure gradient and curvature effects induced by the geometry of the body in a very confined region, turbulence destruction and even transfer from turbulence kinetic energy to momentum energy occurs based on experimental observations. The linear eddy-viscosity turbulence model fails to predict such flow phenomena completely. Reynolds stress transport models can provide a better prediction, but energy backward transfer from turbulence kinetic energy to momentum energy is not predicted. It is desirable that

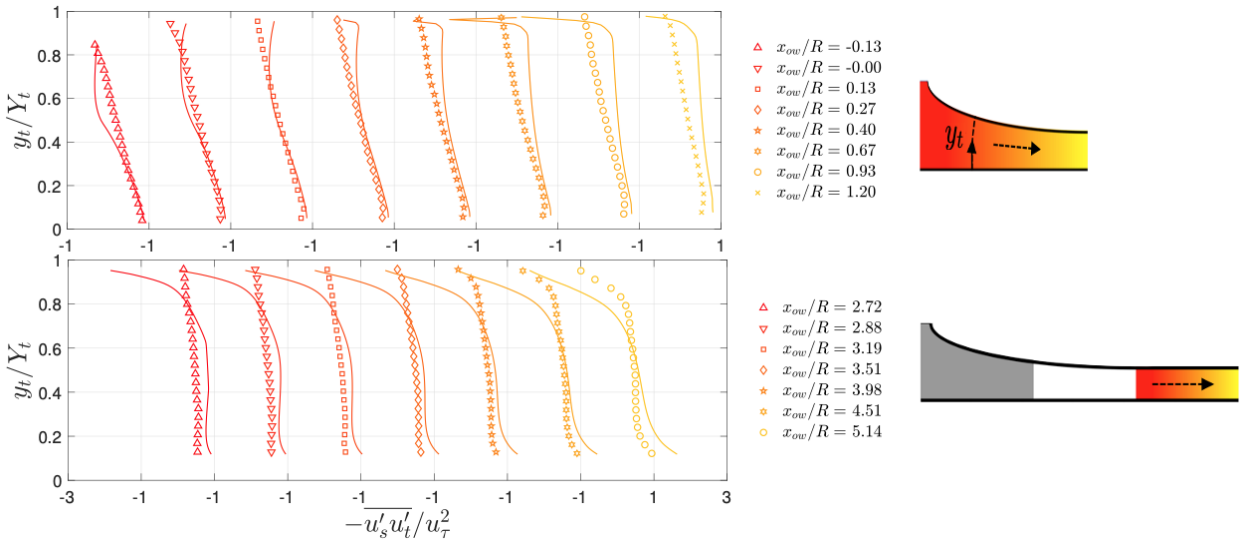

Fig. 12 Preliminary computations using OpenFOAM v6 with the k-ω-SST model by [19]. Shear stress comparisons over the bow and mid-body of the case with $d/D = 1/3$.

more detailed measurement be made in this region in future so that the physics of the flow in this important region can be better understood, especially for the shear stress. It is crucial to confirm that energy backward transfer does occur in this region, which can be characterized by a negative turbulent eddy-viscosity when the shear stress is expressed using the Boussinesq assumption. It is to be expected that the model for the rapid distortion terms will play an important role in this assessment.

One source of the uncertainty in the present simulation comes from the inlet condition used in the CFD simulation. The inlet condition extracted from the computation of fully developed pipe flow does not match very well with the experimental results. A measurement at an upstream section far enough from the body where the pressure gradient due to the body is small will be very useful to calibrate the inlet condition for CFD simulation in any future study. It would be also very useful to make additional measurements just upstream of the body to investigate the evolution of turbulent flow under the action of adverse pressure gradient before impinging on the body. Due to the very poor prediction in the bow region, the assessment of turbulence modelling in the other parts of the flow becomes very difficult. Overall, it seems that the more complex SSG-LRR Reynolds stress transport equation model does not provide better predictions compared with the simple SST linear eddy-viscosity model, except in the bow region where it clearly shows its superiority. One possible way to avoid this difficulty is to perform a simulation with a computational domain starting from a mid section of the body where the inlet condition is prescribed based on the measurement data. However, imposing an appropriate inlet condition in this way is not an easy task, especially for turbulent quantities such as turbulent dissipation.

Acknowledgments

The experimental work was supported by ONR under Grant N00014-17-1-2309 (Program Manager Peter Chang).

References

[1] Ding, L., Saxton-Fox, T., Hultmark, M., and Smits, A. J., "Effects of pressure gradient and streamline curvature on the statistics of a turbulent pipe flow," *Proc. Turbulence and Shear Flow Phenomena 11*, University of Southampton, Southampton, UK, 2019, p. 353.

[2] Queutey, P., and Visonneau, M., "An interface capturing method for free-surface hydrodynamic flows," *Computers & Fluids*, Vol. 36, No. 9, 2007, pp. 1481–1510.

[3] Moonesun, M., Korol, Y. M., Dalayeli, H., Tahvildarzade, D., Javadi, M., Jelokhaniyan, M., and Mahdian, A., "Optimization on submarine stern design," *Proceedings of the Institution of Mechanical Engineers, Part M: Journal of Engineering for the Maritime Environment*, Vol. 231, No. 1, 2017, pp. 109–119.

[4] McKeon, B. J., Swanson, C. J., Zagarola, M. V., Donnelly, R. J., and Smits, A. J., "Friction factors for smooth pipe flow," *Journal of Fluid Mechanics*, Vol. 511, 2004, pp. 41–44.

[5] Fuchs, T., Hain, R., and Kähler, C. J., "Non-iterative double-frame 2D/3D particle tracking velocimetry," *Experiments in Fluids*, Vol. 58, No. 9, 2017, p. 119.

[6] Kähler, C. J., Scharnowski, S., and Cierpka, C., "On the uncertainty of digital PIV and PTV near walls," *Experiments in Fluids*, Vol. 52, No. 6, 2012, pp. 1641–1656.

[7] Agüera, N., Cafiero, G., Astarita, T., and Discetti, S., "Ensemble 3D PTV for high resolution turbulent statistics," *Measurement Science and Technology*, Vol. 27, No. 12, 2016, p. 124011.

[8] Ding, L., and Smits, A. J., "Relaxation of turbulent pipe flow downstream of a square bar roughness element," *Journal of Fluid Mechanics*, Vol. 922, 2021.

[9] Ahn, J., Lee, J. H., Lee, J., Kang, J.-h., and Sung, H. J., "Direct numerical simulation of a 30R long turbulent pipe flow at Re τ= 3008," *Physics of Fluids*, Vol. 27, No. 6, 2015, p. 065110.

[10] Vallikivi, M., Hultmark, M., Bailey, S. C. C., and Smits, A., "Turbulence measurements in pipe flow using a nano-scale thermal anemometry probe," *Experiments in fluids*, Vol. 51, No. 6, 2011, pp. 1521–1527.

[11] Leroyer, A., and Visonneau, M., "Numerical methods for RANSE simulations of a self-propelled fish-like body," *Journal of Fluids and Structures*, Vol. 20, No. 7, 2005, pp. 975–991.

[12] Deng, G. B., and Visonneau, M., "Comparison of explicit algebraic stress models and second-order turbulence closures for steady flows around ships," *In 7th International Conference on Numerical Ship Hydrodynamics*, Vol. 10, 1999, p. 5953.

[13] Duvigneau, R., and Visonneau, M., "On the Role Played by Turbulence Closures in Hull Shape Optimization at Model and Full Scale," *J. Mar. Sci. Technol.*, Vol. 8, 2003, pp. 11–25.

[14] Cécora, R.-D., Radespiel, R., Eisfeld, B., and Probst, A., "Differential Reynolds-Stress Modeling for Aeronautics," *AIAA Journal*, Vol. 53, No. 3, 2015, pp. 1–17. Published online: 10 September 2014, March 2015.

[15] Guilmineau, E., Deng, B., G, Leroyer, A., Queutey, P., Visonneau, M., and Wackers, J., "Assessment of Hybrid RANS-LES Formulations for Flow Simulation around the Ahmed Body," *Computers & Fluids*, Vol. 176, 2015, pp. 302–319.

[16] Visonneau, M., Guilmineau, E., and Rubino, G., "Local Flow around a Surface Combatant at Various Static Drift Conditions: The Role Played by Turbulence Closures," *33rd Symposium on Naval Hydrodynamics*, Osaka, Japan, 2020, p. 65.

[17] Wackers, J., Deng, G. B., Guilmineau, E., Leroyer, A., Queutey, P., and Visonneau, M., "Combined refinement criteria for anisotropic grid refinement in free-surface flow simulation," *Computers & Fluids*, Vol. 92, 2014, pp. 209–222.

[18] Mozaffari, S., Guilmineau, E., Visonneau, M., and Wackers, J., "Average-based mesh adaptation for hybrid RANS/LES simulation of complex flows," *Computers & Fluids*, Vol. 232, 2022, p. 105202.

[19] Menter, F. R., "Two-equation eddy-viscosity turbulence models for engineering applications," *AIAA Journal*, Vol. 32, No. 8, 1994, pp. 1598–1605.

[20] McKeon, B. J., Li, J., Jiang, W., Morrison, J. F., and Smits, A. J., "Further observations on the mean velocity distribution in fully developed pipe flow," *J. Fluid Mech.*, Vol. 501, 2004, pp. 135–147.

[21] Allen, J. J., Shockling, M. A., and Smits, A. J., "Evaluation of a universal transitional resistance diagram for pipes with honed surfaces," *Phys. Fluids*, Vol. 17, 2005, p. 121702.

[22] Gunady, I. E., Ding, L., Hultmark, M., and Smits, A. J., "Response of Turbulent Pipe Flow to an Axisymmetric Body," *Bull. American Physical Society*, 2021.